MDPI

Article

An Experimental and Numerical Study of Motion Responses of Multi-Body Arrays with Hinge Connections

De-Qing Zhang [1], Zhi-Ming Yuan [2], Guang-Wei Zhao [2], Yu-Jing Chen [1] and Jun-Feng Du [1,*]

[1] College of Engineering, Ocean University of China, Qingdao 266100, China; zhangdeqing@ouc.edu.cn (D.-Q.Z.)
[2] Department of Naval Architecture, Ocean & Marine Engineering, University of Strathclyde, Glasgow G4 0LZ, UK
* Correspondence: dujunfeng@ouc.edu.cn

Abstract: Hinged multi-body systems are gaining popularity in the field of ocean engineering. Their performance is commonly evaluated using numerical simulations, but comparisons with experimental data are required to ensure the accuracy of the computational tools. However, there is a dearth of experimental studies on the motion performance of hinged multi-body systems, particularly those involving more than two hinged floating bodies. This study aims to fill this gap in experimental data for hinged multi-body systems beyond two bodies. The rectangular box was chosen as the test model due to its stable hydrodynamic properties and ease of numerical modelling. Five identical boxes were prefabricated and subsequently tested in the pool in a sequence ranging from one to five boxes to capture the motion performance. Additionally, a numerical programme based on potential flow theory was developed for mutual validation with the experimental data. Firstly, the physical properties of each box were determined through equations calculation and a free decay test, enabling the acquisition of all parameters for conducting numerical simulations. Then, the response amplitude operator (RAO) curves for the heave and pitch motion of a single box were depicted, and the results indicated that the resonant frequency in pitch direction obtained from the regular wave test was consistent with that obtained from the free decay test. Finally, the motion RAO curves of hinged multi-body systems were presented and analysed. The agreement between the measured and computed results confirms the suitability of the experimental data presented in this study as benchmark data for validating numerical simulations.

Keywords: model test; multi-body arrays; hinge connections; motion responses; response amplitude operator

1. Introduction

Multi-body systems are emerging as a highly appealing solution for ocean clean energy production and marine space utilisation [1]. In these multi-body arrays, hinge constraints are commonly imposed between adjacent structures to mitigate the risk of collisions or separation [2,3]. Unlike arrays of multiple structures with independent oscillations, these hinged systems are subject not only to hydrodynamic interactions among different bodies but also to significant mechanical coupling effects caused by the connectors.

There is a growing body of literature that explores the practical application of hinged multi-body arrays in engineering. Diamantoulaki and Angelides [4] conducted a study on the performance of various configurations of hinged floating breakwaters. They compared the responses of these hinged structures to those of a single floating breakwater without hinges and found that adding more hinge joints enhanced the performance of the breakwater system, except at very low and very high frequencies. Rogne [5] focused on the modelling and simulation of a hinged 5-body wave energy converter (WEC), which consists of a shallow draft cylindrical centre floater hinged to 4 semi-submerged spherical buoys.

One significant design feature of this WEC is that the hinges are submerged, resulting in a diagonal-like mode of motion for the buoys. Jiang et al. [6] studied the hydrodynamic performance of an artificial island composed of hinged multi-modules. They also investigated the hydrodynamic sensitivity of such multi-body structures to the number and arrangement of modules, as well as the incident wave angle. Ma et al. [7] investigated the dynamic responses of a hinged floating aquaculture array subjected to regular waves. This study indicated that the maximum pitch response is predominantly influenced by the rotational stiffness of the hinge joint. Overall, the operational performance of these hinged multi-body systems is strongly linked to the dynamic performance of individual structures.

Numerical simulation plays a vital role in accurately analysing the dynamics of multi-body arrays with hinge constraints, primarily due to its notable advantages in terms of time efficiency and practicality. These numerical simulations are commonly conducted utilising various numerical techniques, which enable precise prediction of the motion responses of hinged systems. Newman [8] was the first to consider the effect of hinge constraints in multi-body systems. He applied a generalized mode method to calculate the dynamic responses of a two-barge system connected by hinge joints. A Lagrange multiplier technique was used by Sun et al. [9] to study the same hinge problems. Zheng et al. [10] calculated the motions of hinged multi-body systems in the frequency domain by incorporating a constraint matrix. Both latter studies validated their findings against Newman's result and achieved strong agreement. Compared to numerical simulations, physical model tests can offer more convincing results as they directly measure the behaviour of the system under realistic conditions. Therefore, experimental data is commonly employed to validate the accuracy of the numerical techniques. Jiang et al. [11] conducted both experimental model tests and numerical simulations to examine the capability of a potential-flow solver in predicting the motions and loads on hinged two-module systems. The study concluded that the solver's application is limited due to the lack of implicit consideration of flow viscosity and strong nonlinear free-surface typologies. Jin et al. [12] conducted an experimental study of a 1:25 scale-designed hinged raft WEC to explore the physical performance and to investigate the effect of nonlinear energy dissipations like viscosity, submergence, and overtopping. Their aim is to update an open-source tool WEC-Sim, to enable it to model any two-body hinged WECs. Unfortunately, there is currently a scarcity of experimental research on the motion performance of hinged multi-body systems, particularly with respect to data involving more than two hinged floating bodies. Moreover, for an experimental test to serve as a benchmark test for validating the accuracy of numerical procedures, it is essential that the study can be easily reproducible. However, this aspect is often overlooked in current experimental studies.

The aim of this paper is to provide benchmark data for validating numerical simulations of the motion results of multi-body systems with hinge connections. Specifically, the study measures the motion results of a hinged system with up to 5 hinged rectangular boxes in a pool, filling the gap in experimental data for hinged multi-body systems beyond two bodies. The accuracy in hinged multi-body computation of our in-house numerical solver, MHydro, is also validated through comparison with the experimental data. The paper is structured as follows. Section 2 describes the model tests of hinged multi-body systems carried out at the University of Strathclyde. Section 3 outlines the numerical methodology used to mutually validate the experimental results. The measurement results of motion responses are presented in Section 4, and finally, the conclusions are drawn in Section 5.

2. Model Test Description

To obtain the benchmark data for validating numerical simulations of a hinged multi-body system, model tests were conducted in a 3-D compact wave tank at the Kelvin Hydrodynamic Laboratory of the University of Strathclyde [13]. The principal dimension of this tank is $9 \times 3.15 \times 1.36$ m. Figure 1 shows a photo of the wave tank. The tank is equipped with 8 flap paddles as the wave maker to generate regular or irregular waves. Four position-fixed wave probes were placed around the physical model to measure the

wave elevation history. The time history of each model's movements in 6 degrees of freedom (DoFs) was recorded using a Qualisys motion capture system [14]. The present displacement measurement system included several groups of markers, three high-speed cameras, and a non-contact optical Qualisys tracking system. These markers are covered with special materials so they can strongly reflect the infrared rays emitted by the cameras. Four retro-reflective markers were attached to the upper surface of one physical model to establish a local coordinate system, which will move with the model. Two high-speed cameras were positioned above the wave maker, and another one was located near the wave absorber to cover as much pool area as possible. As shown in Figure 2, several vertical mesh panels composed of iron wires are installed at the end of the wave tank to dissipate the transmitted waves. Each grid plate is arranged diagonally, with the vertical edges of adjacent plates tightly fitted together to form a serrated wave-absorbing device. This design ensures effective wave attenuation across the entire width of the tank's end. Additionally, the serrated device is filled with absorbing material to enhance wave energy dissipation.
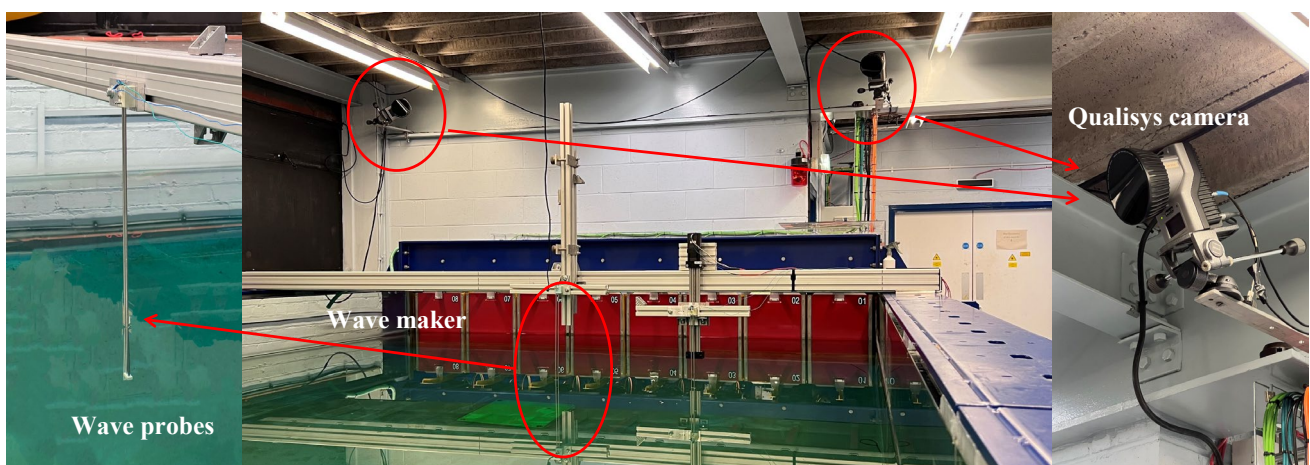

Figure 1. Photo of wave tank and Qualisys camera.

Figure 2. Wave absorbing device at the end of the wave tank.

Five series of tests were designed here, varying only in the number of hinged floating bodies from 1 to 5. The physical model was designed as a rectangular box with identical geometry dimensions and physical properties due to its ease of numerical modelling. The

main physical parameters of the model are presented in Table 1. The incident wave direction was defined as $\beta = 180°$, with an incident wave amplitude of 0.01 m. Taking the hinged 5-body array as an example, a schematic of the physical experiment is shown in Figure 3. The origin of the global coordinate system was fixed at the calm water surface at the tank centre, and the positive *x*-axis pointed to the wave maker. Regardless of the number of floating bodies in the physical model system, the centre of the entire model system at rest was located at the origin of the global coordinate system, and the positions of the four-wave probes remained constant. A horizontal mooring was attached to each corner of the entire model system to provide extra restoring forces, ensuring that the models could return to their initial positions after the wave maker ceased operation. Figure 4 shows the hinge assembly used to connect two adjacent bodies. Two hinges were symmetrically assembled along the longitudinal direction on the upper surface of the adjacent models, with the hinge rotation axis located at the midline of the gap. The other three multi-body model systems in the test were also connected by the same hinge assembly between adjacent boxes. To prevent relative movement between the hinge joint and the attached box, three holes were arranged in a triangular pattern on one side of the hinge unit. These holes are used for inserting screws and connecting the bodies. The distance between two adjacent box models could be adjusted by changing different holes in the hinge. However, since the aim of these tests is to provide benchmark data on the motion performances of hinged multi-body arrays for the validation of numerical simulations rather than conducting a parametric study, only the results with a fixed gap distance $d_b = 0.08$ m are presented in this study. Additionally, to ensure that the centre of gravity and the centre of buoyancy of each floating box are aligned as 0 in the horizontal plane of the body-fixed coordinate system and the models were half submerged in still water. Varying sizes of weights were used for ballasting.
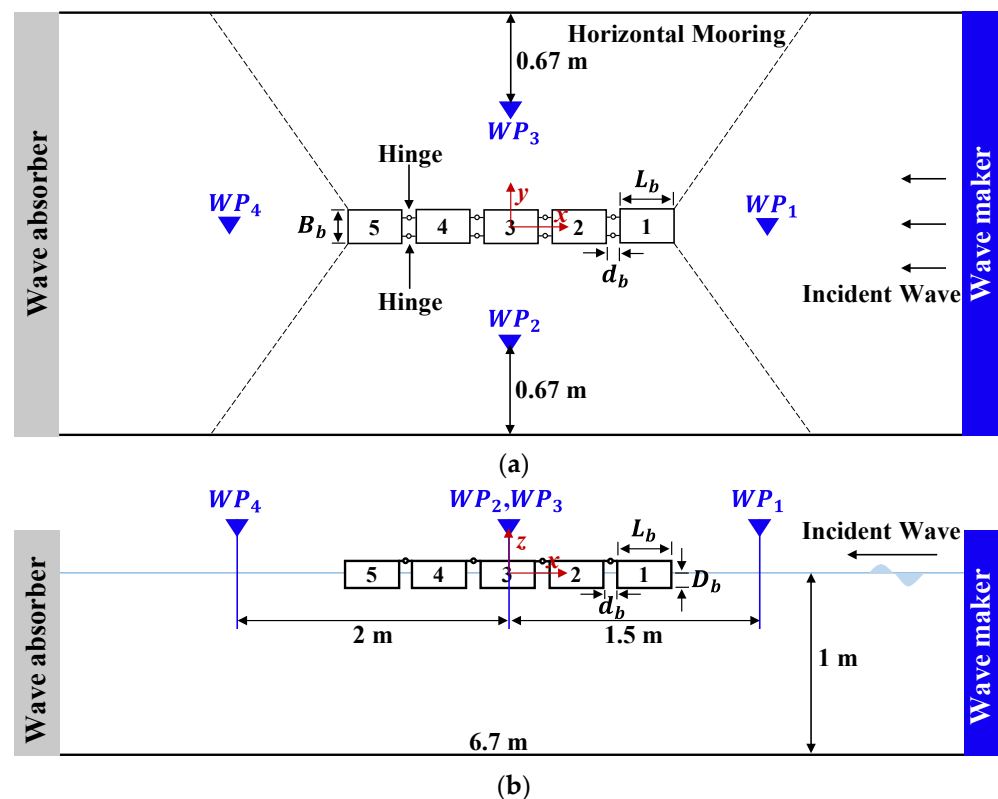

Figure 3. Schematic diagram of the experimental setup for hinged multi-box arrays, taking a 5-box array as an example. The test system consists of 1, 2, 3, 4 and 5 boxes respectively, with the entire test system arranged in the middle of the test tank. (**a**) Top view; (**b**) Side view.
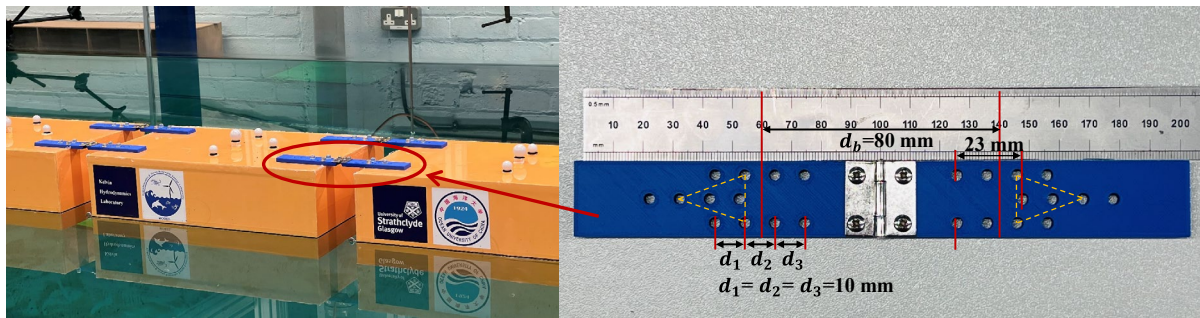
Figure 4. Photos of the multi-boxes and hinge assemblies with a gap distance d_b = 80 mm. The gap between adjacent boxes can be adjusted by repositioning the fixing holes.

Table 1. Principal physical parameters of the box model.

Parameters	Units	Values
Length L_b	m	0.4
Width B_b	m	0.25
Height D_b	m	0.2
Draft h_b	m	0.1
Mass m_b	kg	10

3. Numerical Modelling

To enhance the credibility of the benchmark data obtained from the present model test, numerical simulations using the same geometrical cases as those used in the test were conducted. The results of the numerical simulations were then compared with the experimental data for validation. These simulations were performed using MHydro [15], an in-house code developed using potential flow theory and the 3-D Rankine source panel method. Here, we will provide a brief overview and validation of the methodology, while more detailed information on how MHydro was employed to solve the problem of hydrodynamic interactions and motion characteristics of hinged arrays can be found in Zhang et al. [15].

3.1. Numerical Methodology

Figure 5 illustrates the corresponding right-handed coordinate systems for N bodies hinged together and oscillating in open sea conditions. The origins of the body coordinate systems $o^m–x^m y^m z^m$ (where m = 1, 2, ..., N) are situated on the calm water surface at midships, with the positive $o^m–z^m$ axis oriented upwards. The wave incident direction β is the angle between the direction of wave propagation and the positive X-axis. $\beta = 180°$ is applied in the present study.

The fluid surrounding the system is assumed to be ideal, and its flow is described by the velocity potential that satisfies the Laplace equation. The velocity potential within the fluid domain can be represented as

$$\Psi(\vec{X}, t) = Re[\eta_0 \varphi_0(\vec{X})e^{-i\omega_0 t}] + Re\sum_{j=1}^{6}\sum_{m=1}^{N}[\eta_j^m \varphi_j^m(\vec{X})e^{-i\omega_0 t}] + Re[\eta_7 \varphi_7(\vec{X})e^{-i\omega_0 t}] \quad (1)$$

where N is the total number of hinged structures; ω_0 is the frequency of the incident wave; φ_0 is the unit incident potential and $\eta_0 = \eta_7$ is the incident wave amplitude; φ_j^m is the unit radiated velocity potential in 6 DoFs and η_j^m is the corresponding displacement amplitude (η_1: surge; η_2: sway; η_3: heave; η_4: roll; η_5: pitch; η_6: yaw); φ_7 is the unit diffracted velocity potential. Generally, the governing equation and linearised boundary conditions for the diffraction and radiation problems can be solved as
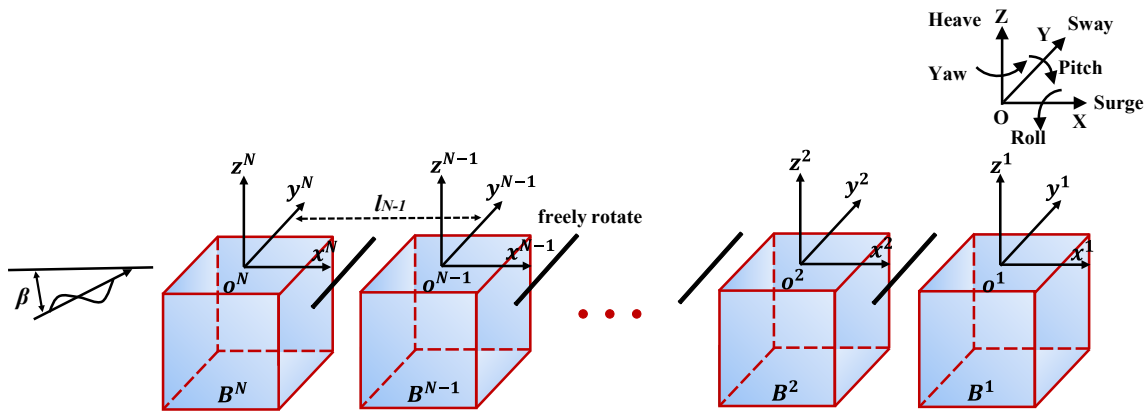
Figure 5. Coordinate system.

(1)   Diffraction wave potential

$$\nabla^2 \varphi_7 = 0 \quad \text{in the fluid domain;} \tag{2}$$

$$g\frac{\partial \varphi_7}{\partial z} - \omega_0{}^2 \varphi_7 = 0 \text{ on the undisturbed free surface } S_f; \tag{3}$$

$$\frac{\partial \varphi_7}{\partial n} = -\frac{\partial \varphi_0}{\partial n}\Big|_{S_m} \text{ on the mean wetted body surface } S_m; \tag{4}$$

$$\frac{\partial \varphi_7}{\partial z} = 0 \quad \text{on the seabed.} \tag{5}$$

(2)   Radiation wave potential

$$\nabla^2 \varphi_j^m = 0, \ j = 1, 2, \ldots, 6 \ \text{ in the fluid domain;} \tag{6}$$

$$g\frac{\partial \varphi_j^m}{\partial z} - \omega_0{}^2 \varphi_j^m = 0, \ j = 1, 2, \ldots, 6 \text{ on the calm water surface } S_f; \tag{7}$$

$$\frac{\partial \varphi_j^m}{\partial n} = \begin{cases} -i\omega_0 n_j|_{S_m} \\ 0|_{S_{others}} \end{cases},$$

$$j = 1, 2, \ldots, 6 \quad \text{on the mean wetted body surface } S_m \ (B^m \text{ is oscillating while others are fixed)}; \tag{8}$$

$$\frac{\partial \varphi_j^m}{\partial z} = 0 \quad \text{on the seabed.} \tag{9}$$

To fully address the boundary value problem, it is necessary to apply an appropriate Sommerfeld radiation condition to the control boundary.

Once the unknown diffraction and radiation velocity potential are obtained, the pressure on the wet surface of each structure can be calculated using Bernoulli's equation,

$$p_j^m = -i\omega\rho\varphi_j^m \tag{10}$$

where ρ denotes the density of the surrounding fluid. Then, the wave excitation forces acting on the floating bodies can be derived as

$$F_i^{W_m} = \iint\limits_{S_m} (p_0 + p_7) n_i dS \tag{11}$$

The radiation hydrodynamic forces can be expressed as

$$F_i^{R_m} = \sum_{j=1}^{6} \iint_{S_m} p_j^m n_i dS \cdot \left(\sum_{n=1}^{N} \eta_j^n \right) = \sum_{j=1}^{6} \sum_{n=1}^{N} \left(\omega_0^2 \mu_{ij}^{mn} + i\omega_0 \lambda_{ij}^{mn} \right) \eta_j^n,$$
$$i = 1, 2, \ldots, 6; \ m = 1, 2, \ldots, N \tag{12}$$

where μ_{ij}^{mn} and λ_{ij}^{mn} are the added mass and damping coefficients.

The presence of hinge constraints in the multi-body system causes the motion response of all modules to be coupled rather than independent. If a hinge constraint is applied along the y-axis, as shown in Figure 6, only pitch motion remains free, while the other five DoFs are constrained to ensure the continuity of these motions at the hinge point. Thus, five constraints exist between the interconnected adjacent bodies, specified by the following equations

$$\eta_1^m + \eta_5^m z^m - \eta_6^m y^m = \eta_1^{m+1} + \eta_5^{m+1} z^{m+1} - \eta_6^{m+1} y^{m+1}$$
$$\eta_2^m - \eta_4^m z^m + \eta_6^m x^m = \eta_2^{m+1} - \eta_4^{m+1} z^{m+1} + \eta_6^{m+1} x^{m+1}$$
$$\eta_3^m + \eta_4^m y^m - \eta_5^m x^m = \eta_3^{m+1} + \eta_4^{m+1} y^{m+1} - \eta_5^{m+1} x^{m+1} \tag{13}$$
$$\eta_4^m = \eta_4^{m+1}$$
$$\eta_6^m = \eta_6^{m+1}$$

where (x^m, y^m, z^m) and $(x^{m+1}, y^{m+1}, z^{m+1})$ represent the coordinates of the hinge joint in coordinate systems fixed on the adjacent bodies, respectively. The frequency motion equation for the hinged multi-body array can be expressed as

$$\begin{bmatrix} -\omega_0^2(M + \mu) + i\omega_0(\lambda + C) + K & D_J^T \\ D_J & 0 \end{bmatrix} \begin{Bmatrix} \eta \\ F_J \end{Bmatrix} = \begin{Bmatrix} F^W \\ 0 \end{Bmatrix} \tag{14}$$

where M is the mass matrix of $(6N \times 6N)$; K is the stiffness matrix; μ is the added mass matrix, and λ is the damping matrix, both with dimensions $(6N \times 6N)$; C is the viscous damping matrix of $(6N \times 6N)$; D_J is the displace constraint matrix with dimensions $(Q \times 6N)$, where Q represents the hinge number; η is the motion response matrix of size $(6N \times 1)$; F_J is the vector of internal forces at the hinge joint, with dimensions $(Q \times 1)$; and F^W is the wave excitation force matrix, also of size $(6N \times 1)$. In the array mass matrix M, the mass matrix of the m-th body is placed in the position of rows $6(m-1)+1$ to $6m$ and columns $6(m-1)+1$ to $6m$. The definition of the array stiffness matrix K is the same as that of the array mass matrix. The mass and restoring stiffness matrix of the m-th floating body can be expressed as

$$M_{ij}^m = \begin{bmatrix} m_a & 0 & 0 & 0 & m_a z_G & 0 \\ 0 & m_a & 0 & -m_a z_G & 0 & m_a x_G \\ 0 & 0 & m_a & 0 & -m_a x_G & 0 \\ 0 & -m_a z_G & 0 & M_{44} & 0 & M_{46} \\ m_a z_G & 0 & -m_a x_G & 0 & M_{55} & 0 \\ 0 & m_a x_G & 0 & M_{64} & 0 & M_{66} \end{bmatrix} \tag{15}$$

$$K_{ij}^m = \begin{bmatrix} 0 & 0 & 0 & 0 & 0 & 0 \\ 0 & 0 & 0 & 0 & 0 & 0 \\ 0 & 0 & \rho g A_w & \rho g M_{wx} & -\rho g M_{wy} & 0 \\ 0 & 0 & \rho g M_{wx} & \rho g(I_{w1} + V z_B) - m_a g z_G & -\rho g M_{wxy} & \rho g V x_B + m_a g x_G \\ 0 & 0 & -\rho g M_{wy} & -\rho g M_{wxy} & \rho g(I_{w2} + V z_B) - m_a g z_G & -\rho g V y_B + m_a g y_G \\ 0 & 0 & 0 & 0 & 0 & 0 \end{bmatrix} \tag{16}$$

where m_a is the body mass; (x_G, y_G, z_G) is the centre of gravity; (x_B, y_B, z_B) is the centre of buoyancy; M_{44}, M_{55} and M_{66} are the roll, pitch and yaw moments of inertia; A_w is the water plane area; M_{wx} and M_{wy} are the first moment of the water plane about the x-axis

and *y*-axis, respectively; M_{wxy} is the second moment about the *x*–*y* plane; I_{w1} and I_{w2} are the second moments of the water plane around the *x*-axis and *y*-axis, respectively; and *V* represents the underwater volume.
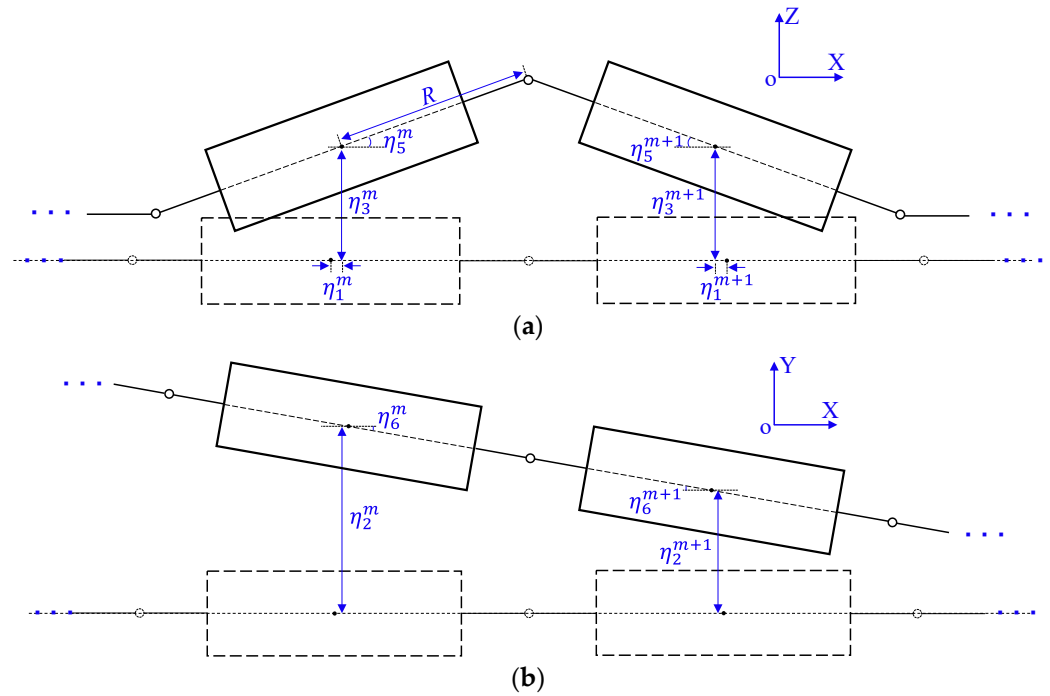

Figure 6. Sketch of multiple bodies with hinge connections. (**a**) Side view; (**b**) top view.

3.2. Validation of the Numerical Methodology

Before comparing the results obtained by the model tests and numerical simulations, it is crucial to conduct a rigorous validation of the numerical programme. Unfortunately, only very limited motion data of hinged multi-body systems is available from the published resources. This further underscores the importance and necessity of conducting the present study.

A problem of two hinged rectangular barges, previously solved using numerical methods with a mode expansion technique by Newman [8] and a boundary element method with a Lagrange multiplier technique by Sun et al. [9], serves as a common benchmark to validate the accuracy of the numerical programme. The configuration and principal dimensions are shown in Figure 7. The geometry of two barges is identical, where the length L_{b2}, the width B_{b2} and the draft D_{b2} of each barge are 40 m, 10 m, and 5 m, respectively. The detailed mass matrix M_{ij}^B and stiffness matrix B_{ij}^B of each barge are expressed as

$$
M_{ij}^B = \begin{bmatrix}
2.050e^6 & 0 & 0 & 0 & 0 & 0 \\
0 & 2.050e^6 & 0 & 0 & 0 & 0 \\
0 & 0 & 2.050e^6 & 0 & 0 & 0 \\
0 & 0 & 0 & 2.135e^7 & 0 & 5.949e^{-8} \\
0 & 0 & 0 & 0 & 2.776e^8 & 0 \\
0 & 0 & 0 & 5.949e^{-8} & 0 & 2.904e^8
\end{bmatrix}
$$

$$
K_{ij}^B = \begin{bmatrix}
0 & 0 & 0 & 0 & 0 & 0 \\
0 & 0 & 0 & 0 & 0 & 0 \\
0 & 0 & 4.018e^6 & -1.183e^{-1} & -1.270e^1 & 0 \\
0 & 0 & -1.183e^{-1} & -1.675e^7 & 0 & 0 \\
0 & 0 & -1.270e^1 & 0 & 4.858e^8 & 0 \\
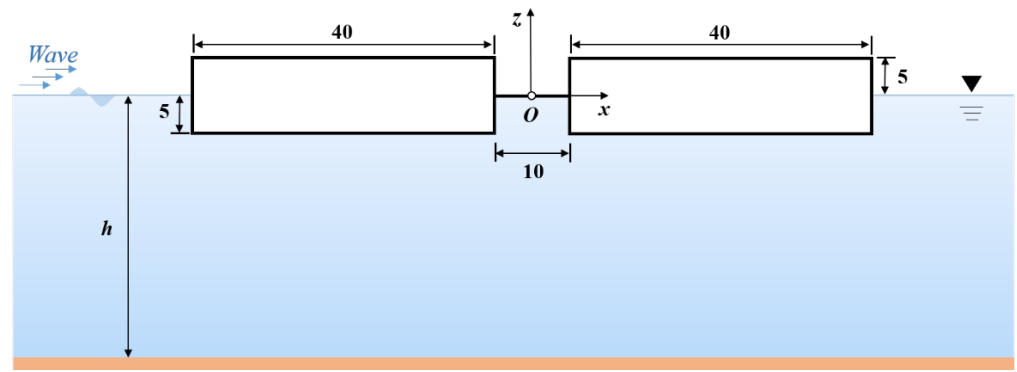0 & 0 & 0 & 0 & 0 & 0
\end{bmatrix}
$$

Figure 7. Configuration of the hinged barges.

The gap between two barges is 10 m, and the water depth is assumed to be infinite. A hinge is located at the horizontal midline of the gap to connect the two separated barges and to allow the barges to rotate about the horizontal hinge axis. The response amplitudes of the hinge motions and the vertical internal forces exerted on the hinge are shown in Figure 8. To compare the results given by the present model with the published results, the vertical motion amplitude of the hinge ξ_3 is non-dimensionalized by A, while the hinge rotation α is non-dimensionalized by $2kA$. Here kA is the wave steepness. And the vertical force in the hinge is non-dimensionalized by $\rho g A L_{b2} B_{b2}$. Although differences with the motion results published by Newman [8] can be found below the wave period $T = 6$ s, the present motion and force results are in very satisfactory agreement with those of Sun et al. [9]. The discrepancy with Newman's results could be attributed to the different values taken for the wave period spacing, where no periods were taken between 5 s and 6 s in Newman's results. It indicates that the present in-house programme is applicable to predict the hinge motions and forces.
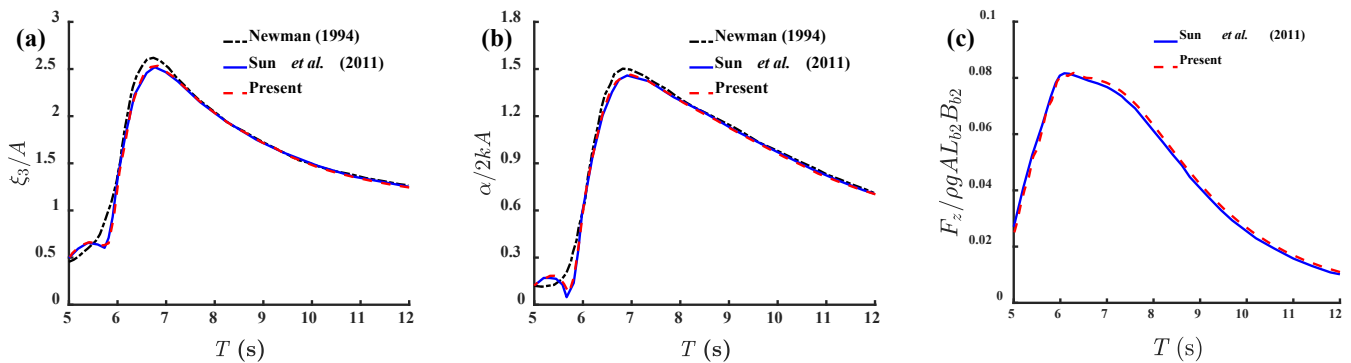

Figure 8. Motions of the hinge and vertical force in the hinge. (**a**) Vertical motion at the hinge; (**b**) relative rotation of the hinge; (**c**) vertical force acting in the hinge [8,9].

4. Results and Discussions

Compared to numerical simulations, the results obtained from physical model tests are generally considered to be more convincing and trustworthy. This is due to the fact that physical model tests directly observe and measure the behaviour of the system under real-world conditions, providing tangible and empirical evidence of its performance. Detailed information on the present hinged multi-body model test and comparison with numerical simulations will be described in this section. It is important to note that the pitch results for the five-body array with hinge connections have been previously reported as validation data by Zhang et al. [15]. However, the heave and pitch experimental results for the single floating body, as well as the hinged two-, three-, and four-body arrays, are presented for the first time in this paper. Additionally, the heave results for the hinged five-body array are also reported here for the first time.

4.1. Physical Properties of Single Box

In the present study, with the incident wave angle set to $\beta = 180°$ for a head wave condition, six DoFs for each structure's motion can be simplified to just three: surge, heave, and pitch. Thus, the mass and restoring stiffness in the roll and yaw direction are not provided in the present study. However, since the horizontal displacement can be affected by the four horizontal moorings imposed on the model system, the focus is primarily on the heave and pitch motions.

To obtain numerical results of the heave and pitch motion, the mass and restoring stiffness in these two directions should be determined. Since each floating box is half submerged in still water, as shown in Figure 9, the centre of buoyancy in the *z*-direction is at $z_B = -0.05$ m. The centre of gravity in the *z*-direction is measured through an incline test using a swing set, as shown in Figure 10. Figure 11 shows a schematic diagram of the swing cline test. The upper part of the swing is equipped with horizontal cutters at the front and back along the *y*-axis, supported at the origin *o*. After the physical model is placed in the swing, both the swing and the model are supported by the cutters and can swing freely around the *y*-axis of the support point. The dotted lines illustrate the initial positions of the swing and the physical model at rest. G_1 represents the position of the centre of gravity of the swing, G_2 is the position of the gravity of the physical model, and G is the position of the centre of gravity of the system consisting of both. A weight of P is placed on the swing at a horizontal distance *d* from the origin *o*, which causes the swing and model system to tile together. According to the principle of moment balance, the coordinate of the centre of gravity of the physical model can be obtained by

$$Pd\cos\theta = -z_{G1}W_1\sin\theta - z_{G2}m_b\sin\theta \tag{17}$$

where θ is the angle at which the swing tilts after the weights are placed; W_1 is the weight of the swing; z_{G1} is the z-coordinate of the swing; z_{G2} is the z-coordinate of the physical model; m_b is the mass of the physical model.
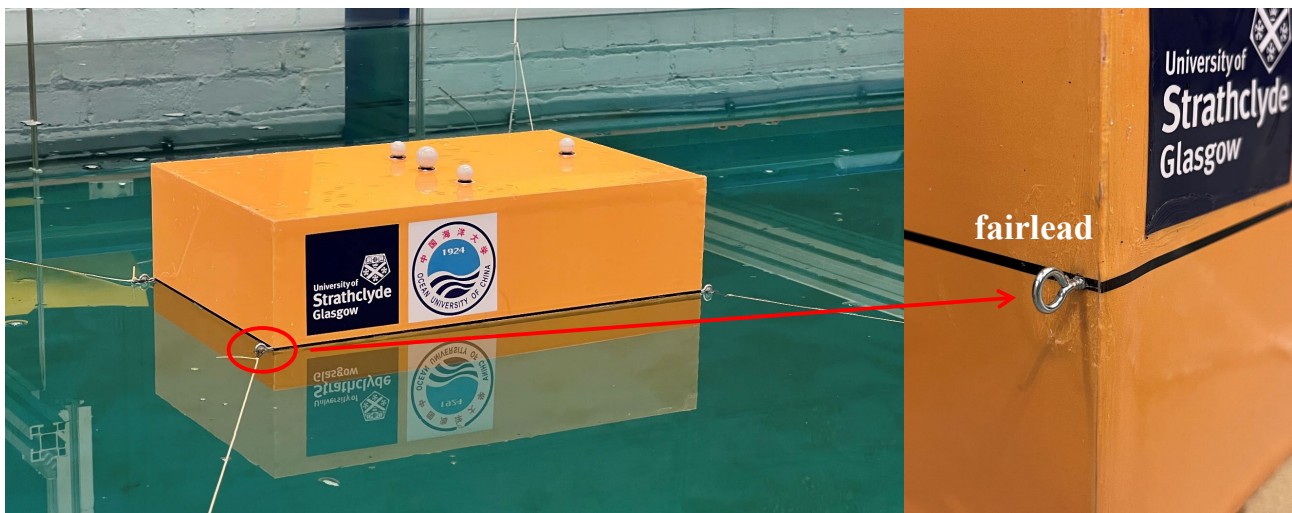

Figure 9. Photo of the single box.
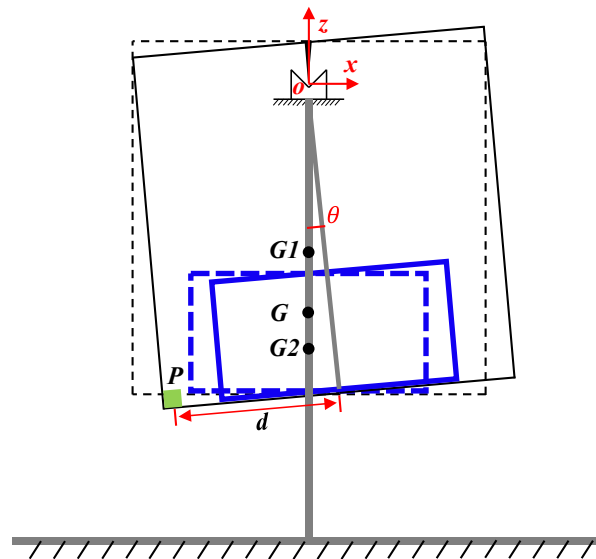
Figure 10. Photo of the swing set.

Figure 11. Schematic diagram of the swing incline test. The dotted lines represent the initial positions of the swing and the physical model at rest, and the solid lines indicate their positions after a weight have been added.

Drawing from the swing incline test, the *z*-coordinate of the centre of gravity is confirmed to be $z_G = -0.027$ m in the body-fixed coordinate system. Since the *x*–*y* plane section of the physical model is a standard rectangle, the second moment around the *y*-axis I_{w2} can be derived from

$$I_{w2} = B_b L_b^3 / 12 \tag{18}$$

Once the $I_{w2} = 0.0013 \ m^4$ is obtained, the restoring stiffness in the pitch direction can be calculated by Equation (16), and the result is $K_{55} = 10.4881$ N·m/rad. Moreover, the pitch moment of inertia M_{55} can be derived from the motion equation as given in the following;

$$\omega_{55} = \sqrt{\frac{K_{55}}{M_{55} + \mu_{55}}} \sqrt{1 - \left(\frac{\lambda_{55}}{2\sqrt{M_{55}K_{55}}}\right)^2} \tag{19}$$

where ω_{55} is the natural frequency in pitch direction; μ_{55} and λ_{55} are the added mass and potential damping at this natural frequency, respectively. To determine the natural frequency in pitch, a free decay test in calm water is performed in this direction without

applying any external moorings or other constraints on the model. The test starts by applying an external load to the floating box model to displace it from its static equilibrium position. This load should be applied to the longitudinal midline of the model to induce pitch motion only. Then, after the load is released, the model starts to oscillate about the equilibrium position at its natural frequency. Figure 12 presents the time history of the decaying pitch motion of a single floating box model. It can be found that the values in Figure 12 are small. This is due to the fact that the model used in the test exhibits high restoring stiffness in the pitch direction and a minimal external load applied. Based on the results of the free decay test shown in Figure 12, the natural frequency of the box model in pitch is obtained as ω_{55} = 7.306 rad/s. As a result, the pitch moment of inertia can be confirmed as M_{55} = 0.128 kg·m^2, which is equal to the measured values.
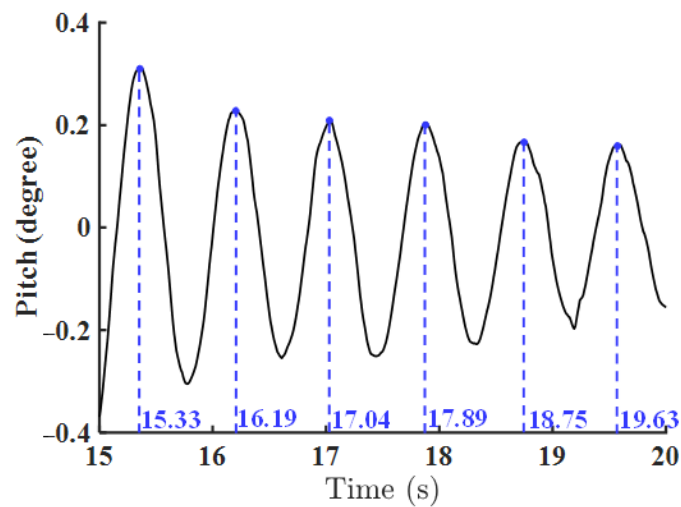

Figure 12. Time history of the pitch motion of a single box in calm water.

Introducing damping terms into numerical simulations enhances the alignment of numerical results with experimental data. The damping of the model structure can be quantified using the following equation:

$$c = 2m_a\omega\xi \tag{20}$$

where ξ represents the logarithmic decrement, defined as

$$\xi = \ln\frac{A_i}{A_{i+1}} \tag{21}$$

where A_i is the *i*-th peak amplitude in the time history of the free decay test, and A_{i+1} is the amplitude of the next peak.

From Figure 12, the damping in the pitch direction is determined as 4.65 N·s·m. Similarly, the damping in the heave direction is calculated to be 10.59 N·s/m.

4.2. Acquisition of Response Amplitude Operators

The amplitude response operator (RAO) is a crucial parameter in the design and response analysis of marine structures. It provides information about how a structure responds to the applied wave forces at different frequencies and is defined as the ratio of the amplitude of the structure's motion to the amplitude of the incident wave. One approach to acquiring motion RAOs for laboratory models is through conducting tests under regular wave conditions. During the regular wave tests, four horizontal moorings are applied to fairleads on the physical model system, as shown in Figure 9, to ensure the system reverts to its initial position once the wavemaker ceases operation. This is achieved by applying additional surge, sway, and yaw restoring forces. To ensure accuracy, data

collection should cover at least 10 wave cycles. This accounts for any transient effects that may occur during the initial cycles and achieves a statistically significant sample size. Figure 13 shows the time series of pitch motions for the single box with a wavemaker frequency of 1.276 rad/s. A Sine function is applied to extract the response information. From this fitting, the amplitude of the response in Figure 13 is calculated to be 0.3847°, with a frequency of 1.2750 rad/s and a phase of −0.034 rad. However, due to the limitations of the wavemaker and tank, replicating the incident wave precisely may not be possible. Thus, it is necessary to record and fit the free surface elevation using a sine function. In this study, limited by the length of the 5-model array, wave probe No.1 (WP1) was positioned too close to the wavemaker, resulting in disturbances in the waves it measured. Therefore, the data collected by wave probe No.2 (WP2) is used for further analysis in the present study.
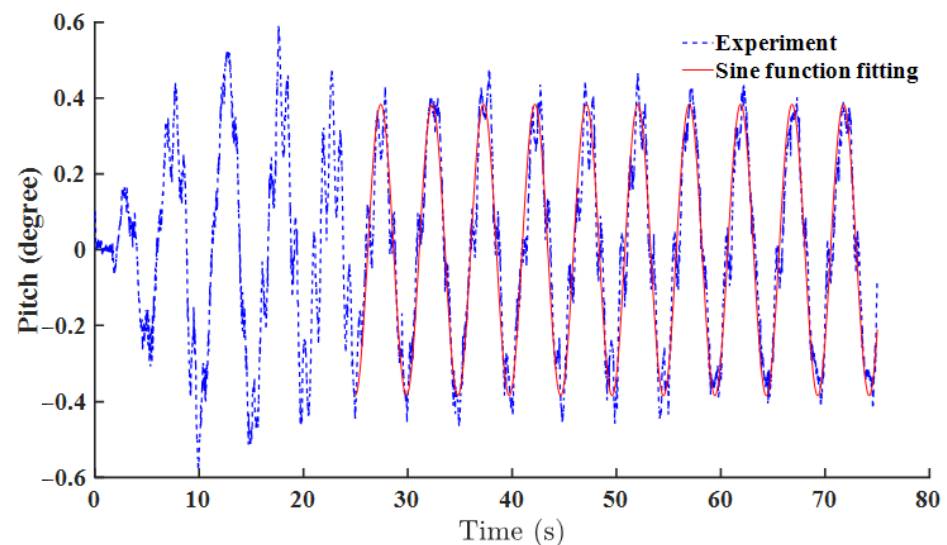

Figure 13. Time history of the pitch motion for a single-box model at a wavemaker frequency of 1.276 rad/s.

Figure 14 shows the panel distribution of the single-box numerical model. The free surface is truncated at 1.5λ upstream, 1.5λ downstream, and $3B_b$ sideward. Figure 15 presents the heave and pitch motion RAOs of the single-box model system. The comparison with the Rankine source panel method is also included. The numerical results presented include two scenarios: one without considering the influence of viscous damping and another that incorporates the effects of viscous damping. To facilitate the comparisons with numerical simulations using the RAO results obtained from the present model test, the units of the parameters in the RAO curves should be unified. The unit of the heave motion RAO is converted to m/m, while the pitch motion RAO is given in rad/m. The wave frequency is presented in rad/s and then non-dimensionalized by $\sqrt{g/L_b}$. It can be observed that the measured and computed results show overall good agreement, particularly between the model test results and the numerical results that incorporate viscous damping effects. Both numerical simulations accurately predict the peak periods. However, the peak values of the numerical results that omit the viscous damping effect are noticeably higher than those of the experimental data. Obvious discrepancies can be observed around wave frequencies of $\omega_0\sqrt{L_b/g} = 0.5$ and 1.45, respectively. Additionally, a small peak can be found at wave frequency $\omega_0\sqrt{L_b/g} = 0.53$ in the measured heave motion RAO and at wave frequency $\omega_0\sqrt{L_b/g} = 0.45$ in the pitch motion RAO from experimental data, respectively. It is likely due to the presence of the fairleads and the moorings. It can also be seen that the resonant frequency is well predicted by the numerical simulations; however, larger motion RAO results are presented compared to the experimental data. These discrepancies are attributed to the exclusion of the viscous effect in the present numerical simulations. Furthermore, the resonant frequency of the single model's pitch motion obtained from the regular wave

tests generally coincides with the natural frequency obtained from the pitch-free decay test, which can be used to mutually verify the accuracy of the model tests.
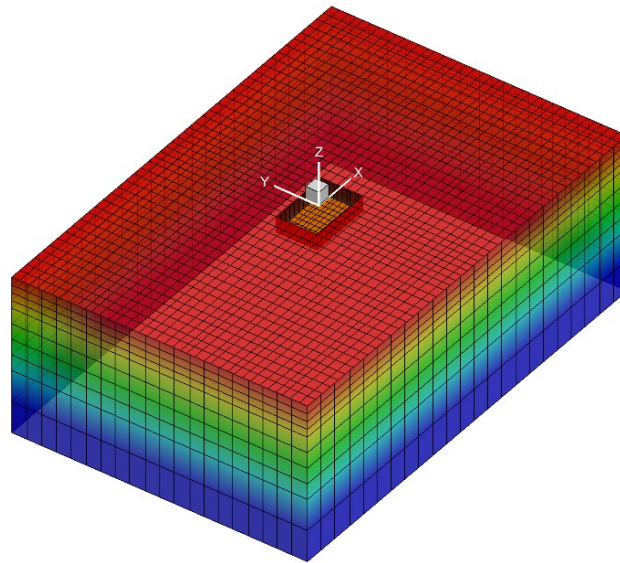

Figure 14. Panel distribution of the single box system with a wavelength of $\lambda/L_b = 2.5$.
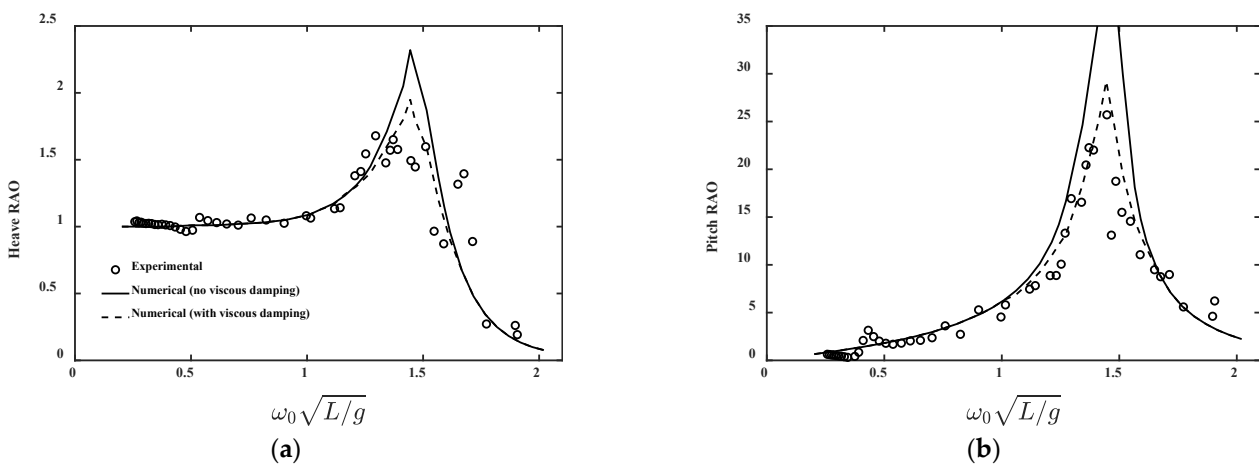

Figure 15. Motion RAOs of the single box system. (**a**) Heave motion; (**b**) pitch motion.

4.3. Motion Responses of Multi-Box Arrays

When calculating the motion response for an array of hinged floating structures, it is crucial to accurately account for both the hydrodynamic interactions between the bodies and the mechanical coupling of the connectors. This obviously differs from the motion response calculation for a single-body system. However, the results obtained from numerical simulations often suffer from errors due to the adoption of certain assumptions, such as the neglect of the fluid viscosity effect. To provide benchmark data for validating computational tools used to evaluate the motion of multi-body arrays with hinge constraints, the motion performance of four multi-body systems with different numbers of floaters are tested separately under regular wave conditions. In this section, the numerical results of hinged multi-body arrays that incorporate the viscous damping effect are presented alongside the experimental data. The viscous damping coefficients are applied only to the main diagonal of the damping matrix.

Figure 16a,c,e,g depict photos of four hinged multi-box model systems, each consisting of a different number of floating bodies in the model systems ranging from 2 to 5. The computational domains and boundary discretization are shown in Figure 16b,d,f,h,

respectively. Figures 17 and 18 present the heave and pitch motion RAOs of four hinged arrays, respectively. It can be seen that the present numerical programme could accurately predict the peak period of the motion responses and roughly predict the peak amplitude. The omission of viscous damping effects outside the diagonal led to incomplete agreement between the predicted amplitudes and the experimental results. It should be noted that for smaller floating bodies, their viscous effects are usually significant, whereas for larger floating structures, the influence of viscous terms is weaker. Keulegan–Carpenter number can be used to quantify the ratio of viscous to inertia force. For small KC numbers, the inertia dominates, while for large numbers, the (turbulence) drag forces are important. However, there is generally good agreement between the measured and computed results, indicating that the model tests and numerical simulation results can be effectively validated against each other. As a result, the present experimental data can serve as benchmark data for other numerical programmes aiming to calculate the motion of hinged multi-bodies. From Figure 17 it can be found that the RAO of the heave motion tends to be 1 at low frequencies in all hinged systems since the floating structures will move with the waves when the wavelength is sufficiently long. With an increasing number of hinged bodies, more peaks appear in the heave and pitch motion RAOs. This can be attributed to the increased interaction among the floaters in systems with more bodies. However, based on the present results, it is not possible to draw a clear conclusion regarding the effect of the number of hinged floaters on the motion responses. This is similar to the findings of Zhang et al. [15], who also reported that a uniform trend for the effect of the number of hinged floaters could not be identified when there were fewer floaters in the hinged multi-body array. They also found that when more than 7 bodies are hinged, the entire array tends to exhibit a consistent trend in heave and pitch motions as the number of floaters continues to increase along the array layout direction.
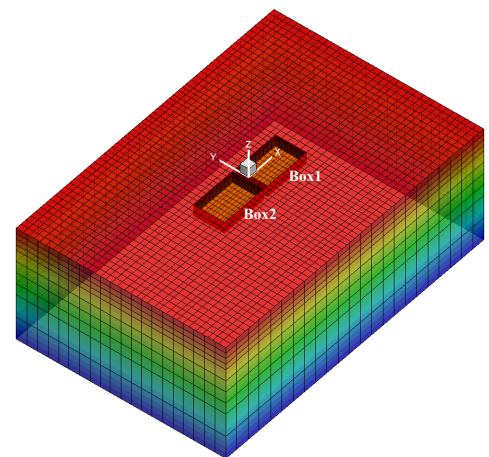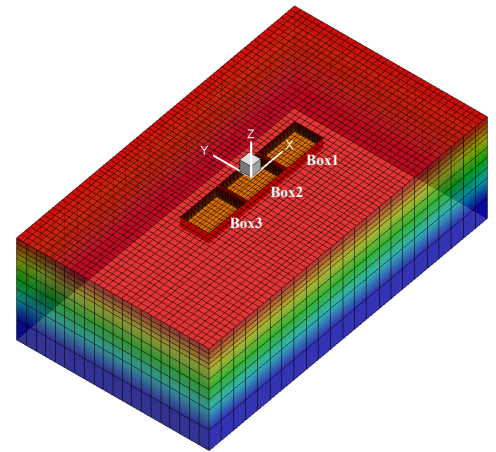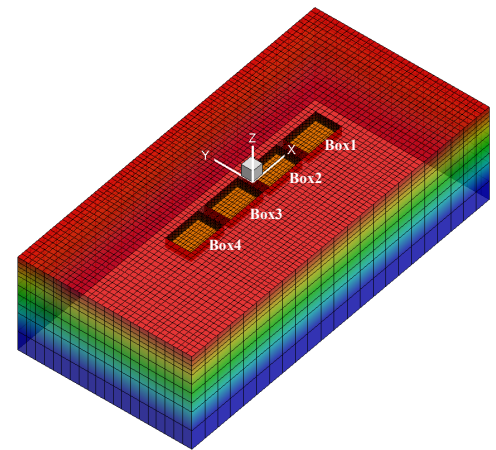

(**a**)   (**b**)

Figure 16. *Cont.*
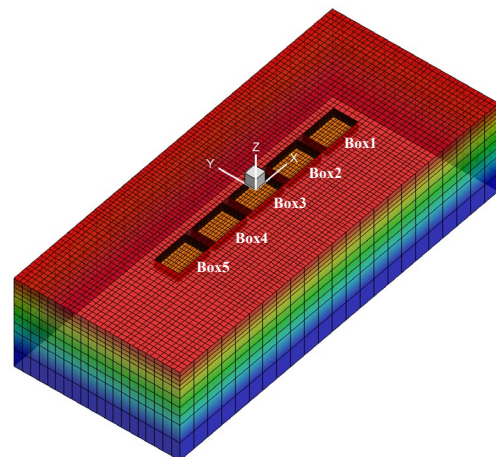
(**c**)

(**d**)

(**e**)

(**f**)

(**g**)

(**h**)

Figure 16. Photos and numerical domains of the hinged multi-box model systems. The numerical domains are at wavelength $\lambda/L_b = 2.5$. (**a**) Photo of the two-box model; (**b**) numerical domain of the two-box system; (**c**) photo of the three-box model; (**d**) numerical domain of the three-box system; (**e**) photo of the four-box model; (**f**) numerical domain of the four-box system; (**g**) photo of the five-box model; (**h**) numerical domain of the five-box system.
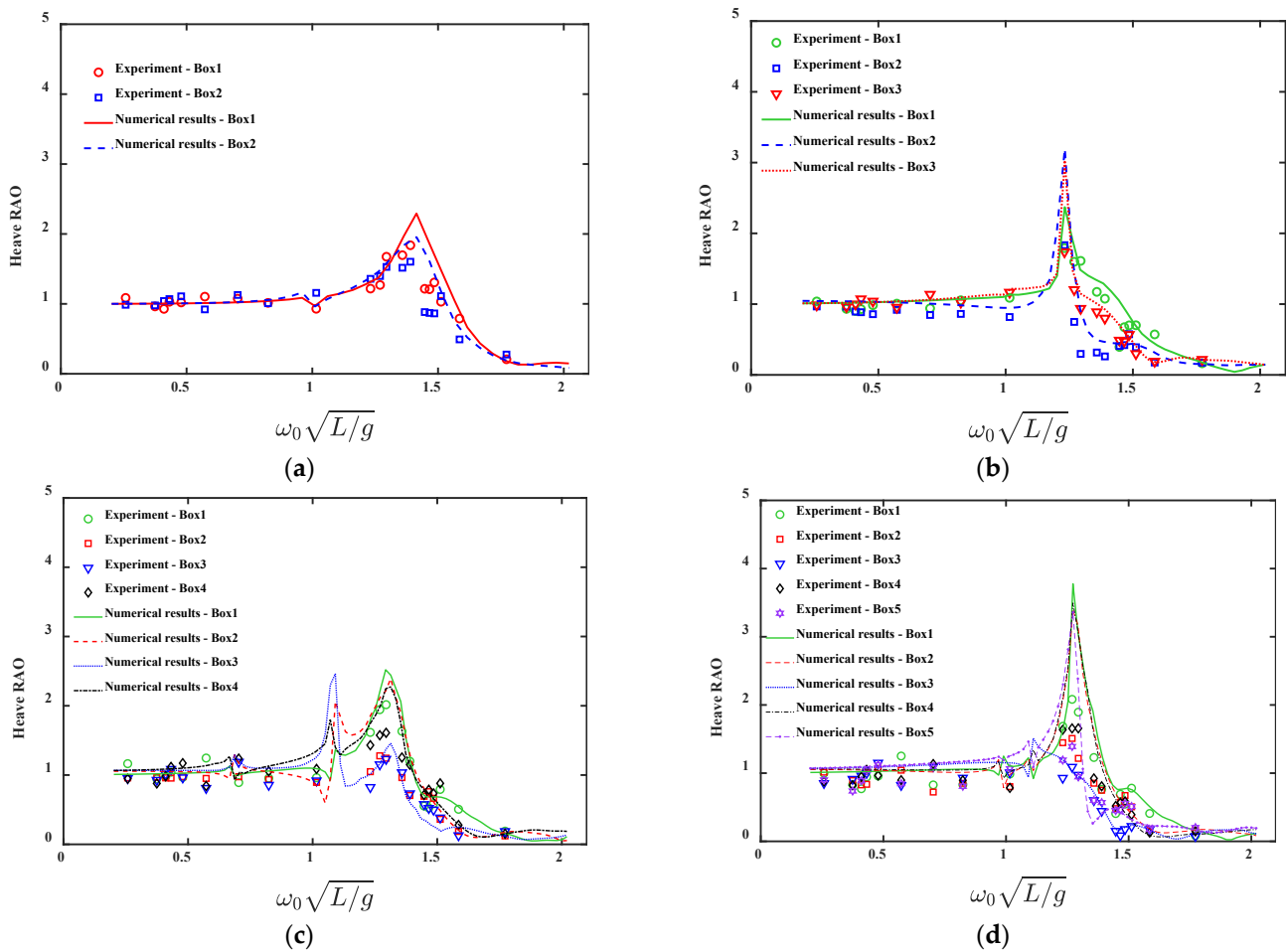
Figure 17. Heave RAOs of the hinged systems. (**a**) Two boxes; (**b**) three boxes; (**c**) four boxes; (**d**) five boxes.
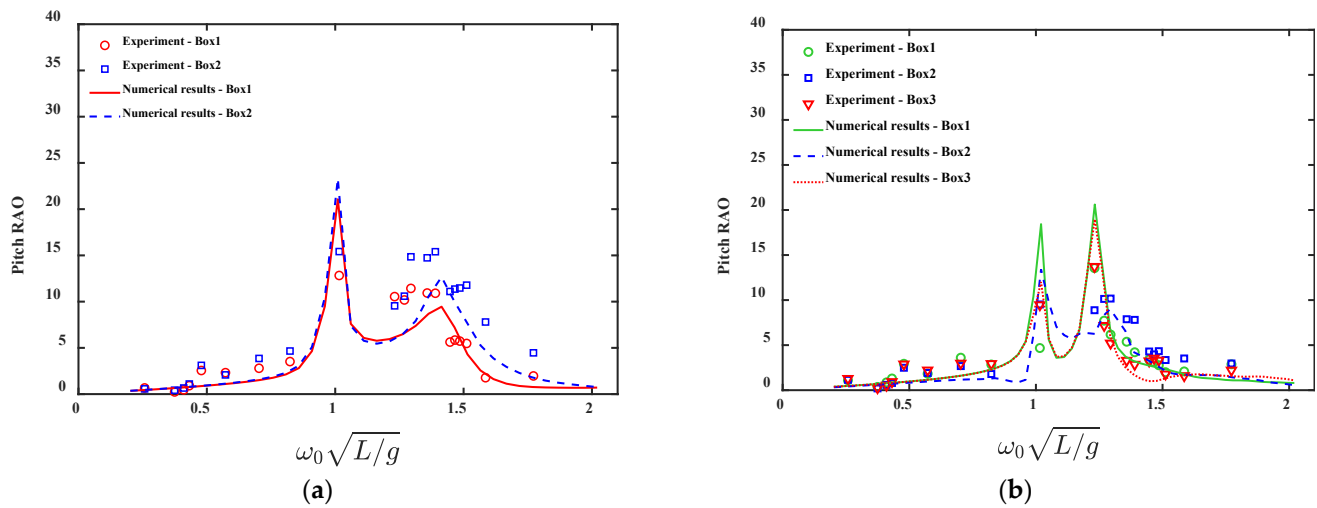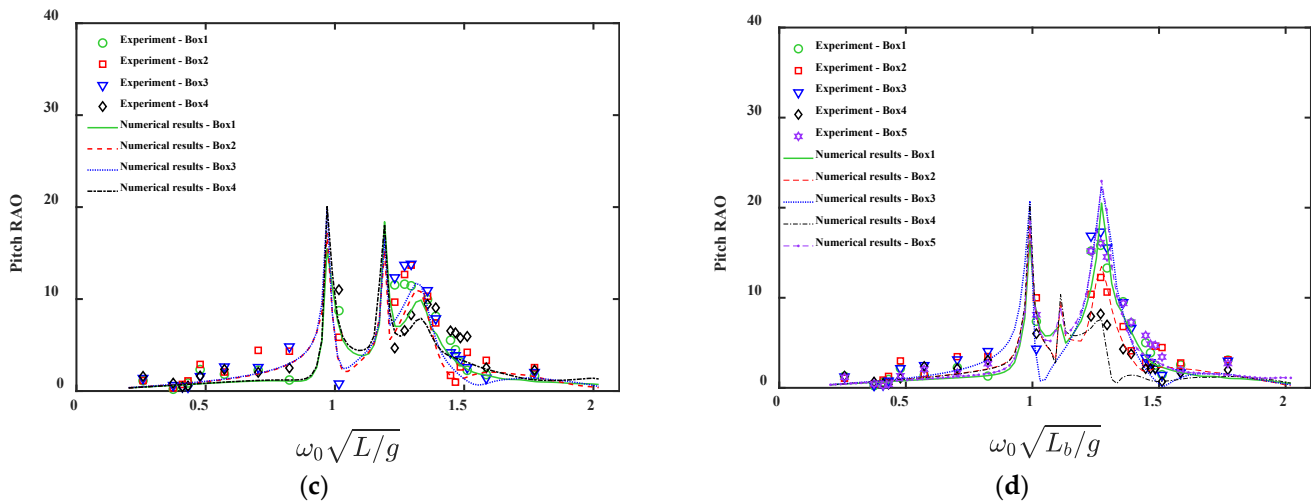
Figure 18. *Cont.*

Figure 18. Pitch RAOs of the hinged systems. (**a**) Two boxes; (**b**) three boxes; (**c**) four boxes; (**d**) five boxes.

5. Conclusions

In this paper, we conducted model tests in a tank at the University of Strathclyde to obtain benchmark experimental data on the motion RAOs of hinged multi-body systems. An in-house code was also developed to calculate the motion RAOs of the same hinged multi-body systems for mutual validation with the experimental data. The models employed in this study were identical rectangular boxes with the same physical properties.

To determine the parameters of the mass, restoring, and viscous damping matrices of the rectangular boxes for numerical simulations, a moment of inertia equation for the rectangular water plane and a free decay test were performed. These procedures were essential to obtain the relevant physical properties and to verify the measured values. An illustrative example is provided using a single-box test under regular waves to explain the process of obtaining the motion RAO of the model from the collected motion time history data. Whether or not viscous damping is considered in numerical simulations, both scenarios can accurately predict the peak period. However, incorporating viscous damping results in peak amplitudes that more closely align with experimental results. Furthermore, the pitch resonant frequency obtained from the single-box regular wave test was consistent with that obtained from the free decay test in pitch motion. Then, hinged model systems consisting of 2 to 5 boxes were sequentially tested under regular waves, and the heave and pitch motion RAOs were presented. Additionally, due to the stability and ease of numerical modelling of the rectangular box, the motion results obtained from the present hinged multi-box model tests can serve as benchmark data to validate other numerical programmes.

Author Contributions: Conceptualization, D.-Q.Z. and Z.-M.Y.; methodology, D.-Q.Z. and J.-F.D.; software, D.-Q.Z.; validation, D.-Q.Z. and G.-W.Z.; formal analysis, D.-Q.Z.; investigation, D.-Q.Z. and Z.-M.Y.; resources, Z.-M.Y.; data curation, G.-W.Z.; writing—original draft preparation, D.-Q.Z.; writing—review and editing, Z.-M.Y., G.-W.Z., Y.-J.C. and J.-F.D.; visualization, D.-Q.Z.; supervision, Z.-M.Y. and J.-F.D.; project administration, Y.-J.C.; funding acquisition, D.-Q.Z. and J.-F.D. All authors have read and agreed to the published version of the manuscript.

Data Availability Statement: The data presented in this study are available on request from the corresponding author.

Conflicts of Interest: The authors declare no conflicts of interest.

References

1. Du, J.; Zhang, D.; Zhang, Y.; Xu, K.; Chang, A.; Zhao, S. Design and comparative analysis of alternative mooring systems for offshore floating photovoltaics arrays in ultra-shallow water with significant tidal range. *Ocean Eng.* **2024**, *302*, 117649. [CrossRef]
2. Chen, M.; Yun, Q.; Hallak, T.S.; Zhou, H.; Zhang, K.; Yang, Y.; Tao, T.; Liu, S.; Jiang, W.; Li, C. Comparative Study on the Performances of a Hinged Flap-Type Wave Energy Converter Considering Both Fixed and Floating Bases. *J. Mar. Sci. Eng.* **2024**, *12*, 1416. [CrossRef]
3. Yu, S.R.; Zhang, M.; Zhang, D.Q.; Yuan, Z.M. Optimal declutching control of hinged multiple floating bodies. *Ocean Eng.* **2024**, *306*, 117992. [CrossRef]
4. Diamantoulaki, I.; Angelides, D.C. Analysis of performance of hinged floating breakwaters. *Eng. Struct.* **2010**, *32*, 2407–2423. [CrossRef]
5. Rogne, Ø.Y. Numerical and Experimental Investigation of a Hinged 5 Body Wave Energy Converter. Ph.D. Thesis, Norwegian University of Science and Technology, Trondheim, Norway, 2014.
6. Jiang, C.; El Moctar, O.; Schellin, T.E. Hydrodynamic sensitivity of moored and articulated multibody offshore structures in waves. *J. Mar. Sci. Eng.* **2021**, *9*, 1028. [CrossRef]
7. Ma, C.; Bi, C.-W.; Xu, Z.; Zhao, Y.-P. Dynamic behaviors of a hinged multi-body floating aquaculture platform under regular waves. *Ocean Eng.* **2022**, *243*, 110278. [CrossRef]
8. Newman, J.N. Wave effects on deformable bodies. *Appl. Ocean Res.* **1994**, *16*, 47–59. [CrossRef]
9. Sun, L.; Taylor, R.E.; Choo, Y.S. Responses of interconnected floating bodies. *IES J. Part A Civ. Struct. Eng.* **2011**, *4*, 143–156. [CrossRef]
10. Zheng, S.M.; Zhang, Y.H.; Zhang, Y.L.; Sheng, W.A. Numerical study on the dynamics of a two-raft wave energy conversion device. *J. Fluid. Struct.* **2015**, *58*, 271–290. [CrossRef]
11. Jiang, C.; El Moctar, O.; Schellin, T.E. Capability of a potential-flow solver to analyze articulated multibody offshore modules. *Ocean Eng.* **2022**, *266*, 112754. [CrossRef]
12. Jin, S.; Wang, D.; Hann, M.; Collins, K.; Conley, D.; Greaves, D. A designed two-body hinged raft wave energy converter: From experimental study to annual power prediction for the EMEC site using WEC-Sim. *Ocean Eng.* **2023**, *267*, 113286. [CrossRef]
13. Zhang, M.; Yuan, Z.M.; Dai, S.S.; Chen, M.L.; Incecik, A. LSTM RNN-based excitation force prediction for the real-time control of wave energy converters. *Ocean Eng.* **2024**, *306*, 118023. [CrossRef]
14. Clemente, D.; Rosa-Santos, P.; Taveira-Pinto, F.; Martins, P. Experimental performance assessment of geometric hull designs for the E-Motions wave energy converter. *Ocean Eng.* **2022**, *260*, 111962. [CrossRef]
15. Zhang, D.; Du, J.; Yuan, Z.; Yu, S.; Li, H. Motion characteristics of large arrays of modularized floating bodies with hinge connections. *Phys. Fluids* **2023**, *35*, 077107.